1	International Journal of Computational Methods
2	(2022) 2250025 (24 pages)

5 © World Scientific Publishing Company

DOI: 10.1142/S0219876222500256



Multiscale Modeling of Metal-Ceramic Spatially 6 Tailored Materials via Gaussian Process Regression 7 and Peridynamics 8 Ahmed El Tuhami 10 Department of Mechanical Engineering The University of Iowa 11 12 Iowa City, Iowa 52242, United States ahmed-eltuhami@uiowa.edu13 Shaoping Xiao* 14 Department of Mechanical Engineering 15 16 Iowa Technology Institute The University of Iowa 17 3131 Seamans Center 18 Iowa City, Iowa 52242, United States 19 $shaoping\hbox{-}xiao@uiowa.edu$ 20 21 Received 22 Revised 23 Accepted 24 Published In this paper, a micro-to-macro multiscale approach with peridynamics is proposed to 25 26 study metal-ceramic composites. Since the volume fraction varies in the spatial domain, 27 these composites are called spatially tailored materials (STMs). Microstructure uncer-28 tainties, including porosity, are considered at the microscale when conducting peridynamic modeling and simulation. The collected dataset is used to train probabilistic 29 30 machine learning models via Gaussian process regression, which can stochastically predict material properties. The machine learning models play a role in passing the infor-31 32 mation from the microscale to the macroscale. Then, at the macroscale, peridynamics is employed to study the mechanics of STM structures with various volume fraction 33 distributions. 34 Keywords: Multiscale; spatially tailored materials; Gaussian process regression; peridy-35

1. Introduction

namics.

36

37

As technology advances in materials science, new generations of composites take 38 the spotlight in day-to-day applications. One set of these next-generation materials 39

^{*}Corresponding author.

2

3

4

5

6

7

8

9 10

11

12

13

14

15

16

17

18

19

20 21

2223

24

25

26

27

28

29

30

31

32

33

34

35

36

37

38

39

40 41

42

is the class of materials known as spatially tailored materials (STMs) [Birman et al. (2008)], also called functionally graded materials (FGMs) [Naebe and Shirvani-moghaddam (2016)]. STMs are composite materials in which the volume fraction of individual material phases varies spatially. In addition to offering the expected benefits of composites, STMs take advantage of their constituent phases in ways that a traditional composite cannot. Particularly, STMs can tailor the thermal and mechanical responses due to the spatial variation (or gradient) in their material properties [Deierling et al. (2021)]. Thus, they have many promising applications in biomedical, defense, and structural engineering [Akshaya et al. (2021)].

There has been a growing interest in titanium-titanium boride whisker (Ti-TiB_w) composites over the past 10 years [Morsi (2019); Morsi and Patel (2007)]. TiB_w reinforcements in the form of particulates or whiskers eliminate the disadvantages of Ti, including poor wear resistance and relatively low stiffness. Many experimental works have been done on this metal-ceramic STM family, including Ti-TiB STMs. Sahay et al. [1999] examined the evolution of microstructure and phases in Ti-TiB composites processed in situ, and they found high-volume fractions of TiB whiskers. In another work, Patil et al. [2019] investigated Ti-6Al-4V alloy with the addition of varying amounts of TiB₂. They discovered that the hardness and wear performance of Ti(Ti-6Al-4V)-TiB₂ were dramatically improved when the weight fraction of TiB₂ was increased. They also observed that the microstructure changed from a martensite lath to a refined bimodal structure. Additionally, they found that the porosity reduced the material density by $1 \sim 2\%$. Shishkovsky et al. [2017] utilized a selective laser melting process to incorporate TiB₂ of submicron sizes to the titanium substrate. They investigated the microstructure via SEM and identified two types of heterogeneity: TiB₂ particles at the interlayer interfaces and element chemical segregation on the boundaries of the tracks.

To study STMs via numerical modeling and simulation, one of the current standard practices is using principles of micromechanics [Ghossein and Lévesque (2012)] and homogenization of representative volume elements (RVEs) to calculate averaged material properties for macroscale simulations. For example, Deierling and Zhupanska [2018] employed finite element method (FEM) simulations with RVEs to estimate graded microstructures' effective spatially varying material properties over a wide temperature range. Then, the estimated material properties were used in macroscale FEM simulations to study thermomechanical responses of STM structures under a combination of thermal and mechanical loading. They also used a similar numerical modeling framework to study metal-ceramic composite panels subjected to high-speed flow [Deierling et al. (2021)]. Xing and Miller [2021] presented a new continuous-discontinuous multiscale modeling approach to failure in quasi-brittle materials to address two major issues of conventional homogenization techniques: macroscale mesh sensitivity and RVE size dependence. However, the homogenization techniques can smear the effects of microstructure uncertainties on material properties.

2

3

4

5

6

8

9

10

11

12

13

14

15

16

17

18

19

20

21

22

23

24

25

26

27

28

29

30

31

32

33

34

35

36

37

38

39

40 41

42

There are other pioneering works in multiscale modeling and simulation of composite materials. Leonetti et al. [2018] proposed a novel multiscale strategy to analyze damage of masonry structures, which were modeled as periodic composites. Their multiscale/multidomain model has an adaptive capability of automatically zooming in on the zones incipiently affected by damage onset. In another work, Trovalusci et al. [2017] presented a two-step multiscale procedure for describing the constitutive behavior of hierarchically structured particle composites. They considered three nested scales (micro, meso, and macro scales) and utilized homogenization techniques for scale transitions. In addition, a combination of molecular dynamics and micromechanics is developed to predict Young's modulus of fullerenereinforced polymer composites [Izadi et al. (2021)]. More works were reviewed in [Trovalusci et al. (2009)] and [Kanouté et al. (2009)].

The above-mentioned works employed either the hierarchical multiscale architecture [Xiao and Yang (2006); Xiao and Yang (2007); Yang and Xiao (2008); Ghaffari et al. (2018)] or the concurrent multiscale strategy [Xiao and Hou (2007)]. Both of them are common approaches to studying the mechanics of composite materials and have benefited from machine learning (ML) and deep learning (DL) recently [Alber et al. (2019)]. Anitescu et al. [2019] and Samaniego et al. [2020] utilized the energy of a mechanical system as the loss function of artificial neural networks (ANNs) in an adaptive collocation strategy to solve partial differential equations for the studies of composites. Liu et al. [2019] proposed a data-driven multiscale method enhanced via a deep material network to approximate complex overall material responses of heterogeneously structured composites. In another study, White et al. [2019] used an ANN-based surrogate model to predict the microscale metamaterial's elastic response and optimize macroscale elastic structures. In addition, Xiao et al. [2019] developed an ML-based multiscale method, in which the datasets collected from molecular simulations were used to train ML regression and classification models for continuum simulations.

Ly et al. [2022] integrated deep learning and genetic algorithm to solve multiobjective optimization problems of laminated functionally graded carbon nanotubereinforced composite quadrilateral plates. Rohit et al. [2021] developed a coupled approach of finite element method and meshfree method with swarm intelligencebased stochastic zero-order search procedure for shape optimization problems. In another work, a combined element-free Galerkin and discrete element methods approach [Wang et al. (2020)] was presented to approximate the interactions between continuum bodies and granular soils. This approach could be an efficient and promising tool to model multiscale, multibody contacting problems. Other recent achievements include a multiscale multi-permeability poroplasticity model [Wang and Sun (2018)], a 3D architecture of deep material networks [Liu et al. (2019)], and a neural-network-assisted multiscale analysis [Balokas et al. (2018)].

This paper proposes a hierarchical multiscale approach, enhanced by probabilistic ML, to study the mechanics of metal-ceramic STM structures via peridynamics.

The contribution of this paper lies in training probabilistic ML models via Gaussian process regression (GPR) to bridge the microscale and the macroscale with the consideration of microscale uncertainties. Recent work by some of the authors [Xiao et al. (2021)] employed a similar approach to study metal-ceramic STM structures via FEM. However, only deterministic predictive models were trained to pass material properties from the microscale to the macroscale. In addition, there was difficulty in generating STM microstructure configurations at volume fractions close to 50%, so only composites with volume fractions less than 25% or greater than 75% were modeled and simulated at the microscale to collect the dataset. This issue is resolved by using peridynamics in this paper. Furthermore, porosity and its uncertainty at the microscale are uniquely considered in this study but not in the previous work [Xiao et al. (2021)].

The outline of this paper is as follows. After the introduction, Sec. 2 describes metal—ceramic STMs, peridynamics, microstructure uncertainties, Gaussian process regression, and the proposed multiscale framework. Section 3 narrates microscale simulations, data collection, and ML model training. Macroscale simulations of STM structures with the implementation of ML predictive models are discussed in Sec. 4, followed by conclusions and a future outlook in Sec. 5.

2. Material and Methodology

2.1. Metal-ceramic spatially tailored materials

We use the metal–ceramic Ti-TiB₂ STM as an example in this paper to illustrate multiscale modeling and simulation of STM structures via the proposed approach. It is common to model an STM as a continuously variable composition material with the volume fractions varying in space. The ceramic volume fraction (CVF), a function of spatial coordinates, is used to distinguish the compositions of two materials (Ti and TiB₂) at a particular material point. It is obvious that Ti is the matrix material when the CVF is less than 50%, and the STM is a metal-like composite material. On the other hand, if the CVF is greater than 50%, the STM is a ceramic-like material since TiB₂ is the matrix material.

Considering a plate made of Ti-TiB₂ in which the volume fraction varies along with the thickness, the CVF, v_f , can be determined via a power-law distribution

$$v_f(z) = v_0 + (v_1 - v_0) \left(\frac{z}{h}\right)^n,$$
 (1)

where z is the depth, and h is the thickness. It is assumed that $v_0 = 0$ and $v_1 = 1.0$ are the CVFs at two surfaces where z = 0 and z = h, respectively. n is the parameter to control the ceramic content distribution. n = 1 is for the linear distribution while n = 2 (quadratic) and 0.5 (square root) are for the nonlinear distributions. The numeric changes of CVF along with the thickness via three different distributions are shown in Fig. 1. In addition, Fig. 2 includes artificially generated images to demonstrate the content changes of Ti (represented via white) and TiB₂ (represented via black) when using different CVF distributions.

2

3

Multiscale Modeling of Metal-Ceramic Spatially Tailored Materials

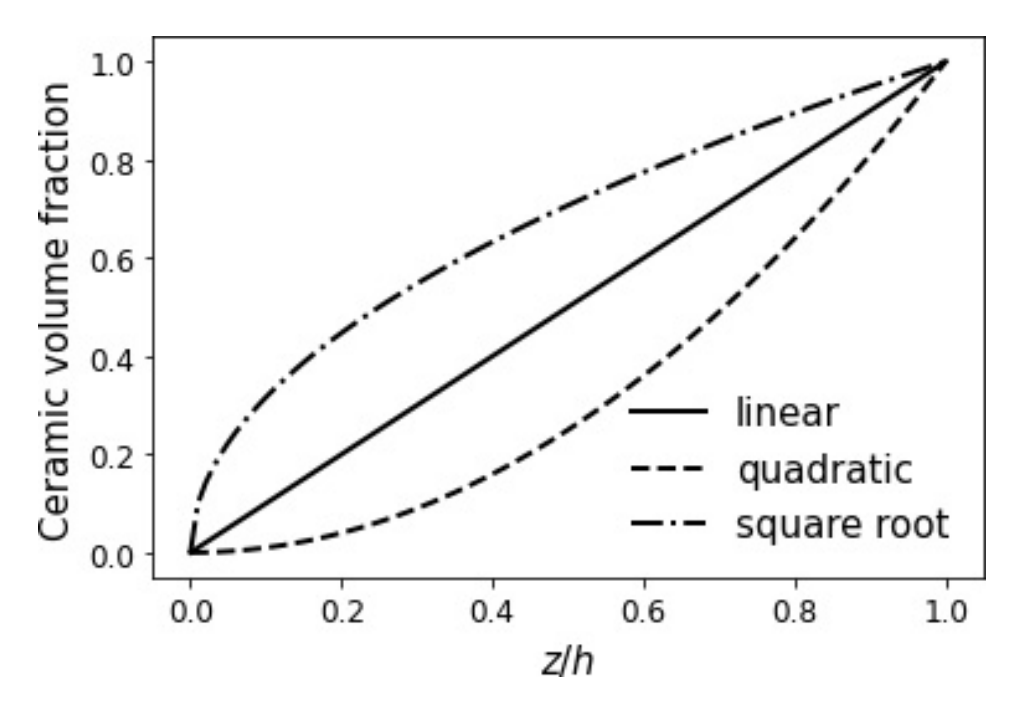


Fig. 1. The ceramic volume fraction distributions.

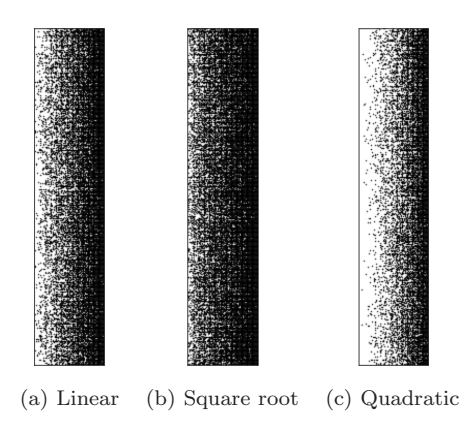


Fig. 2. Artificially generated images of STM with various CVF distributions

It is permissible that the CVF varies in more than one spatial direction. In the case of a two-directional STM structure, the CVF changing in space can be formulated by the following:

$$v_f(x,y) = v_0 + (v_1 - v_0) \left[\eta_x \left(\frac{x}{L} \right)^{n_x} + \eta_y \left(\frac{y}{H} \right)^{n_y} \right],$$
 (2)

where x and y are the coordinates in the horizontal and vertical directions, L and H are the total width and height, and η_i and η_i are parameters controlling the

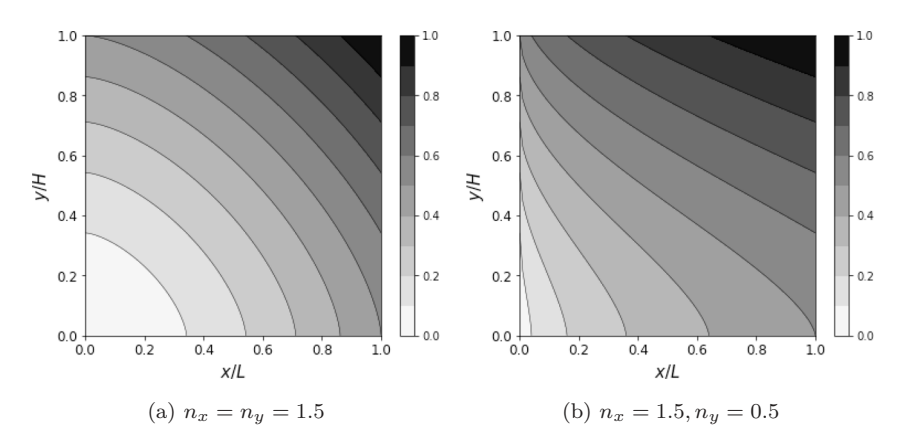


Fig. 3. The contours of CVF distributions in 2D STM plates.

Table 1. Material properties of Ti and TiB₂ at 20°C.

	Young's modulus E (GPa)	Poisson's ratio ν	Density $\rho (kg/m^3)$	Tensile strength σ_t (GPa)
${ m Ti} \ { m TiB}_2$	106.2	0.298	4357	1.17
	495.4	0.100	4505	3.73

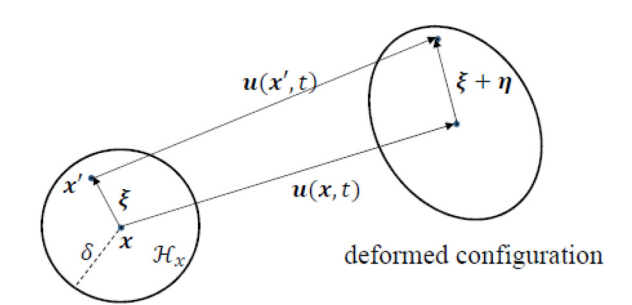
ceramic content and profile in each direction. $v_0 = 0$ and $v_1 = 1$ are the minimum and maximum CVFs, as assumed above. Figure 3 shows the contours of CVFs in 2D plates when two control parameters, n_x and n_y in Eq. (2), are assigned with various values while η_x and η_y are kept as 0.5.

In addition, the material properties of Ti and TiB₂ at room temperature (20 $^{\circ}$ C) are listed in Table 1 according to references [American society for metal (1979); Munro (2000); Wiley *et al.* (1969)].

2.2. Peridynamics

Peridynamic theory [Silling (2000); Silling and Lehoucq (2010)] is a nonlocal model in which the partial differential equations from classical continuum mechanics are reformulated and replaced with integral equations instead. It has been successfully applied to fracture mechanics [Bobaru and Zhang (2015); Silling and Askari (2014)] as well as the studies of plastic deformation [Madenci and Oterkus (2016)], fiber-reinforced composites [Yaghoobi and Chorzepa (2017)], and heterogeneous materials [Jung and Seok (2016)]. Although state-based peridynamics [Silling et al. (2007); Silling (2010)] has been developed, bond-based peridynamics is employed in this paper. In a peridynamic model, the simulation domain is discretized with a number of equally spaced material points. A pairwise bond force vector f is exerted on material point x by material point x', which is in the neighborhood \mathcal{H}_x (with the

Multiscale Modeling of Metal-Ceramic Spatially Tailored Materials



Reference configuration

Fig. 4. The peridynamic bond in the reference and deformed configurations.

- radius δ) of material point x. Figure 4 shows a visual representation of the reference and deformed state of a peridynamics virtual bond between x and x'.
- Correspondingly, a stress divergence term in the equations of motion is replaced by a volume integral of force density as

$$\rho \ddot{\boldsymbol{u}}(\boldsymbol{x},t) = \int_{\mathcal{H}_{\boldsymbol{x}}} \boldsymbol{f}(\boldsymbol{\eta}, \boldsymbol{\xi}, t) dV_{\boldsymbol{x'}} + \boldsymbol{b}(\boldsymbol{x}, t), \tag{3}$$

- where ρ is the density, $\ddot{\boldsymbol{u}}$ is the acceleration vector, and \boldsymbol{b} is the body force vec-
- tor. $\boldsymbol{\xi}$ and $\boldsymbol{\eta}$ are the relative position vector and the relative displacement vector,
- 7 respectively. They are defined as

$$\boldsymbol{\xi} = \boldsymbol{x'} - \boldsymbol{x} \quad \boldsymbol{x'} \in \mathcal{H}_{\boldsymbol{x}} \tag{4}$$

8 and

14

15

16 17

1

2

$$\eta = u(x',t) - u(x,t), \tag{5}$$

- where \boldsymbol{u} is the displacement. Letting $\ddot{\boldsymbol{u}}(\boldsymbol{x},t)=0$ will reduce the peridynamics to peristatics.
- In the naïve peridynamics, the pairwise force density f is calculated based on bond strain s.

$$f(\eta, \xi, t) = cs(\eta, \xi, t), \tag{6}$$

where c is the micromodulus, and

$$s(\boldsymbol{\eta}, \boldsymbol{\xi}, t) = \frac{\|\boldsymbol{\eta} + \boldsymbol{\xi}\| - \|\boldsymbol{\xi}\|}{\|\boldsymbol{\xi}\|}.$$
 (7)

- According to the prototype microelastic brittle (PMB) material model [Silling and Askari (2005)], the critical stretch s_0 for bond failure is introduced. Once the bond is stretched beyond the critical value, bond failure occurs, and the bond is broken.
- The above-mentioned classical formulation is for materials with a Poisson's ratio of 0.25. To model more general materials, Zhu and Ni [2017] considered the effects

of bond rotation, and the reformulated pairwise force density function is rewritten as

$$f(\eta, \xi, t) = csn + \kappa \gamma, \tag{8}$$

- where c is redefined as the first micromodulus while κ is the second micromodulus,
- 4 $n=(\eta+\xi)/\|\eta+\xi\|$ is the current stretch direction, and the shear strain vector γ
- 5 can be calculated as

$$\gamma(\eta, \xi) = \frac{1}{\|\xi\|} \eta \cdot (I - n \otimes n). \tag{9}$$

Given material with Young's modulus E and Poisson's ration ν , the micromoduli in 2D context are derived as

$$c = \frac{6E}{\pi \delta^3 (1 - \nu)}, \quad \kappa = \frac{6E(1 - 3\nu)}{\pi \delta^3 (1 - \nu^2)}$$
 (10)

8 for plane stress problems, and

$$c = \frac{6E}{\pi \delta^3 (1+\nu)(1-2\nu)}, \quad \kappa = \frac{6E(1-4\nu)}{\pi \delta^3 (1+\nu)(1-2\nu)}$$
(11)

9 for plane strain problems.

10

11

12

13

14

15

16

17

18

19

20

21

22

23

24

25

26

27

28

2.3. Gaussian process regression

The ML algorithm used to analyze the datasets in this paper is the GPR, in which the model parameters are random variables. GPR is a Bayesian approach [Gershman and Blei (2012)] to regression when considering both model uncertainty and data uncertainty. It is an attractive ML algorithm because it provides the capability to measure uncertainty in the predictions and be compatible with small datasets. Generally, the Bayesian approach works by specifying a prior distribution, P(w), on the model parameter w, and updating its probability distribution based on the data (X, y) used to train the predictive model. Data has input X and output y. Consequently, the updated distribution P(w | y, X) is the posterior probability distribution and incorporates information from both the prior distribution and the training data. This can be done using Bayes' Rule [Schulz et al. (2018)]:

$$P(\boldsymbol{w} \mid \boldsymbol{y}, \boldsymbol{X}) = \frac{P(\boldsymbol{y} \mid \boldsymbol{X}, \boldsymbol{w}) P(\boldsymbol{w})}{P(\boldsymbol{y} \mid \boldsymbol{X})},$$
(12)

where P(y | X, w) is the likelihood, and P(y | X) is the marginal likelihood or evidence. To get prediction y_* at a point of interest x_* that is not yet observed, the predictive distribution can be calculated by weighting all possible predictions by the posterior distribution of the model parameters.

$$P(y_* \mid \boldsymbol{x}_*, \boldsymbol{y}, \boldsymbol{X}) = \int_{\boldsymbol{w}} P(y_* \mid \boldsymbol{x}_*, \boldsymbol{w}) P(\boldsymbol{w} \mid \boldsymbol{y}, \boldsymbol{X}) d\boldsymbol{w}.$$
(13)

It shall be noted that GPR is a nonparametric method that is not limited by a functional form. GPR can calculate the probability distribution over all admissible functions that fit the data instead of calculating the probability distribution of

parameters for a specific function. Similarly, a prior is set upon the function space, a posterior is calculated using the training data, and the predictive posterior distribution is defined on the points of interest. However, it is common that the prior and likelihood are typically assumed to be Gaussian for the integration to be tractable. With this assumption, the predictive distribution can be calculated. It also follows a Gaussian distribution that provides a point prediction using the mean and the uncertainty quantification using its variance. Consequently, the Gaussian process is similar to an infinite-dimensional multivariate Gaussian distribution.

The approximate function, y = f(x), in GRP is distributed as a Gaussian process

$$f(\mathbf{x}) \sim GP[m(\mathbf{x}), k(\mathbf{x}, \mathbf{x'})]$$
 (14)

which is a distribution over functions and is defined by a mean and a covariance function. The mean function $m(x) = \mathbb{E}[f(x)]$ evaluates the average of all functions in the distribution at the input x. The covariance function, $k(x, x') = \mathbb{E}[(f(x) - m(x))(f(x') - m(x'))]$, represents the dependence between the outputs at different input points x and x'. The covariance function serves as the Gaussian process kernel [Jäkel et al. (2007)], and it is chosen based on the smoothness and likely patterns to be expected in the data. Commonly used kernel functions are the constant, linear, square exponential, and Matern kernels. It is also possible to use a combination of multiple kernels. The kernel used to train the models obtained in this paper is the radial basis function (RBF) kernel, defined as follows:

$$k(x, x') = e^{-\frac{1}{2l^2} ||x - x'||^2},$$
 (15)

where l is the length scale of the kernel as the hyperparameter that must be tuned to the data, and $\|\cdot\|$ is the Euclidean distance.

To conduct regressions by Gaussian process model, the training dataset (X, y) and the predictions y_* at new data points X_* are joint multivariate Gaussian distributed, i.e., normal distribution. This can be expressed as

$$\begin{bmatrix} \boldsymbol{y} \\ \boldsymbol{y}_* \end{bmatrix} \sim \mathcal{N} \left(\begin{bmatrix} m(\boldsymbol{X}) \\ m(\boldsymbol{X}_*) \end{bmatrix}, \begin{bmatrix} \boldsymbol{K} & \boldsymbol{K}_* \\ \boldsymbol{K}_*^T & \boldsymbol{K}_{**} \end{bmatrix} \right), \tag{16}$$

where K = K(X, X), $K_* = K(X, X_*)$, $K_{**} = K(X_*, X_*)$ are the covariance matrices, in which $K_{ij} = k(x_i, x_j)$. It leads to a normal distribution that is defined by the mean and covariance for the prediction

$$y_* | X, y, X_* \sim \mathcal{N}(K_*^T K y, K_{**} - K_*^T K^{-1} K_*).$$
 (17)

The Gaussian process regressor allows for easy prediction of values using the predict function after the model is trained. It is also possible to incorporate independently, identically distribution (i.i.d.) Gaussian noise in the regression model.

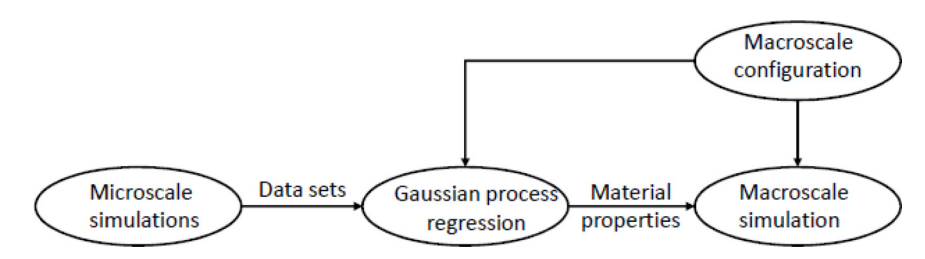


Fig. 5. A microscale/macroscale hierarchical multiscale method.

2.4. Multiscale modeling

A hierarchical multiscale approach enhanced via ML is employed in this paper, as shown in Fig. 5, to study metal–ceramic STM structures. At first, various microstructure configurations at different CVFs are generated considering microstructure uncertainties, especially the uncertainty of porosity. Next, peridynamics simulations are conducted on those microstructure configurations to calculate the material properties, including Young's modulus, Poisson's ratio, and failure strength. Then, GPR models are trained based on the collected dataset to predict those material properties. Finally, given the composite CVF distribution, the material properties at each material point are predicted via the well-trained GPR models at the beginning of macroscale simulations. Consequently, probabilistic ML enhances the message-passing in this hierarchical multiscale method. The process details mentioned above are described in Secs. 3 and 4.

3. Microscale Simulations and Machine Learning

To collect data at the microscale, peridynamics simulations are performed on various material microscale configurations, acting as RVEs, at each given CVF. The dataset is then used to train ML models to predict material properties for macroscale simulations.

3.1. Microscale simulations

The CVF of STM varies spatially at the macroscale. At each macroscale material point, it is assumed that the CVF is a constant at the microscale. All microscale models are generated with 2601 (51 \times 51) material points located within a 30 μ m \times 30 μ m plane. To generate STM microscale configurations, the material points in the simulation domain are randomly assigned as either metal or ceramic according to the given CVF. Although we do not consider the randomness of particle size and orientation [Xiao et al. (2021)], material points can form big particles or whiskers in the generated configuration, especially when the inclusion volume fraction is high enough. Furthermore, as a difference from the work in [Xiao et al. (2021)], the porosity is considered here because a 1% \sim 2% reduction in the material density has been observed in Ti-TiB₂ STM images [Patil et al. (2019)].

Multiscale Modeling of Metal-Ceramic Spatially Tailored Materials

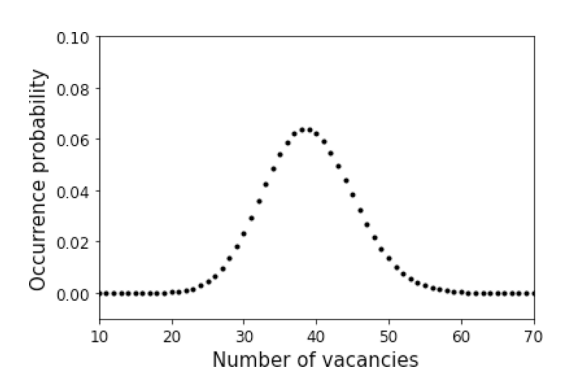


Fig. 6. Occurrence probabilities of the number of vacancies

The addition of porosity into a microscale configuration is performed by randomly removing a small number of material points to generate vacancies in the simulation model. The number of vacancies is determined by the number of Poisson points in a homogeneous Poisson point process [Xiao et al. (2008)]. In a finite two-dimensional plane, the probability of the number (k) of Poisson points (i.e., vacancies or removed material points in this paper) can be written as

$$P(k) = \frac{e^{-\lambda k} (\lambda A)^k}{k!} \quad k = 1, 2, 3, \dots,$$
 (18)

where A is the plane area, and λ is the Poisson point density that is the number of vacancies per area. In this paper, the plane area is $A=900\,\mu\mathrm{m}^2$, and an averaged porosity of 1.5% is chosen. Therefore, $\lambda=0.043\,\mu\mathrm{m}^{-2}$ is defined for the microscale-configuration generation. The probability distribution of the number of vacancies is shown in Fig. 6. It can be seen that, for example, the occurrence probability of 33 vacancies in a generated microscale configuration is 4%. In other words, if a total of 1000 STM configurations are generated for microscale simulations, there are 40 configurations in which 33 material points are randomly selected and removed.

Figure 7 illustrates four microscale STM configurations at different CVFs: 12.5%, 25%, 50%, and 75%. The numbers of vacancies are 48, 46, 40, and 31, respectively. In our previous work [Xiao et al. (2021)], once the number of ceramic particles and the particle sizes were randomly selected, we randomly deposited the particles in the simulation domain before generating meshes. It was difficult to randomly place the particles without overlapping when the CVFs are higher than 25%. Figure 7 shows that the peridynamic model does not suffer the difficulty in configuration generation as indicated in Xiao et al. [2021], especially at the transition from metal-based composites to ceramic-based composites when CVF = 50%. It shall be noted that even at the same CVF various microscale configurations of STM can be generated due to the randomness of inclusion and vacancy locations.

It is assumed that the simulated $30 \,\mu\text{m} \times 30 \,\mu\text{m}$ plane has a thickness of $1 \,\mu\text{m}$, and plane stress problems are considered. In the peridynamic model, $\Delta x = \Delta y = 0.6 \,\mu\text{m}$,

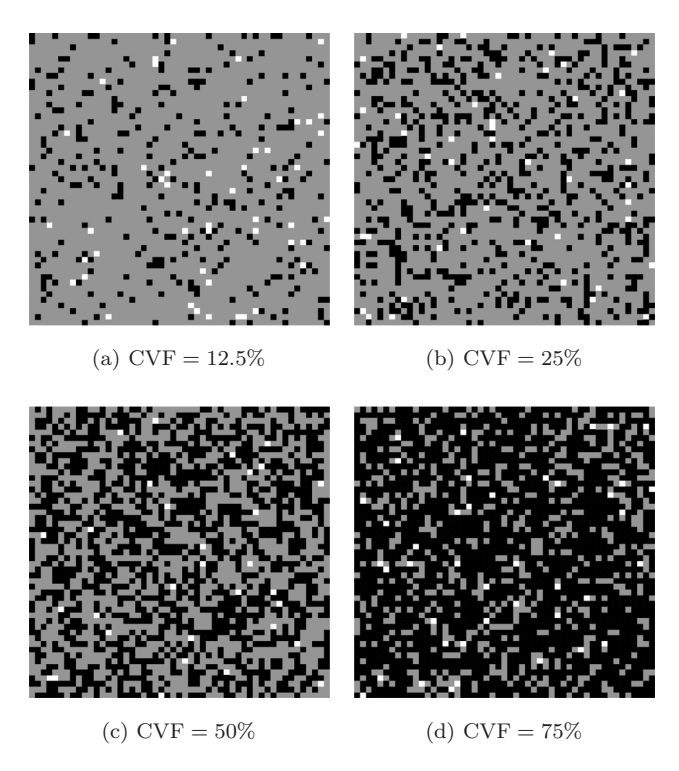


Fig. 7. Microscale configurations of STM with various CVFs (gray represents metal, black represents ceramic, and white represents vacancy).

and the horizon radius $\delta=1.6\Delta x$ is chosen. There are three different types of bonds in the model: metal–metal, ceramic–ceramic, and metal–ceramic. With the material properties listed in Table 1, the first and second micromoduli can be calculated as $c_m=326.01\frac{\rm GPa}{\mu{\rm m}^3},~\kappa_m=47.94\frac{\rm GPa}{\mu{\rm m}^3}$ for metal–metal bonds, and as $c_c=1188.83\frac{\rm GPa}{\mu{\rm m}^3},~\kappa_c=756.53\frac{\rm GPa}{\mu{\rm m}^3}$ for ceramic–ceramic bonds. In addition, the PMB material model [Silling and Askari (2005)] is used with constant values of the critical stretch, $s_{0m}=0.011$ and $s_{oc}=0.008$ for metal–metal and ceramic–ceramic bond failure, respectively. The critical stretches are calculated based on the material tensile strengths. Furthermore, the combining rule is applied to determine the corresponding properties of metal–ceramic bonds: $c_{mc}=\sqrt{c_m c_c}=622.55\frac{\rm GPa}{\mu{\rm m}^3},$ $\kappa_{mc}=\sqrt{\kappa_m \kappa_c}=190.44\frac{\rm GPa}{\mu{\rm m}^3},$ and $s_{0mc}=\sqrt{s_{0m}s_{0c}}=0.0094.$

Peridynamics is employed to conduct the simulations, in which the generated models are subject to the uniaxial tension by applying the prescribed displacement on the top and fixing the bottom. A low strain rate is maintained so that the quasistatic analyses can be approximated by the conducted dynamic simulations. The stress is evaluated at the middle cross-section by dividing the vertical component of the total bond force by the cross-section area. Young's modulus is calculated at 0.005% strain, while Poisson's ratio is determined by the ratio of horizontal to

Multiscale Modeling of Metal-Ceramic Spatially Tailored Materials

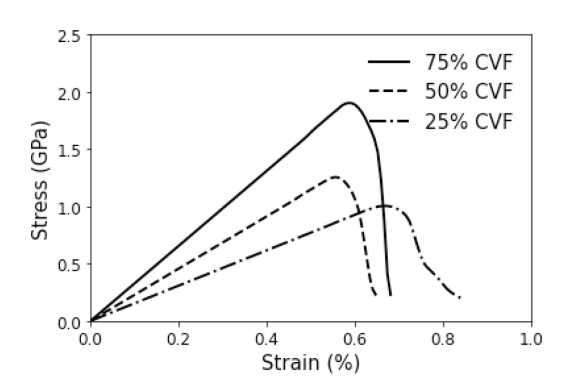


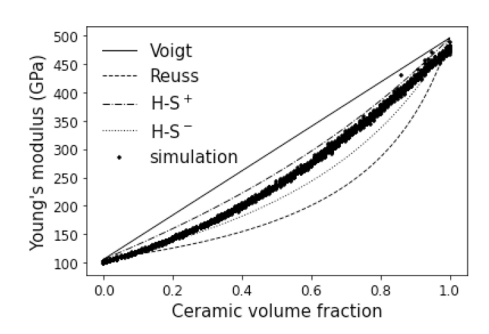
Fig. 8. Stress-strain relationships of composites with various CVFs.

vertical displacements. Since the enforcement of boundary conditions cannot be directly applied on the boundary material points in peridynamics, fictitious walls [Ghaffari *et al.* (2019)] are applied to eliminate such edge softening phenomena [Nishawala and Ostoja-Starzewski (2016)].

Figure 8 illustrates the stress-strain relationships of metal-ceramic STMs with various CVFs. Each stress-strain curve is obtained from one simulation with a randomly generated configuration. Theoretically, the composite with a larger CVF achieves a higher failure strength because the ceramic's failure strength is higher than that of the metal, as shown in Fig. 8. On the other hand, the composite with a higher CVF will have a smaller failure strain because the ceramic's failure strain is smaller than that of the metal. However, due to the microstructure uncertainty, especially the porosity considered in this paper, Fig. 8 shows that the simulated composite with 75% CVF has a bit larger failure strain than the one with 50% CVF. It is worth mentioning that when we conduct more simulations on various configurations for each CVF, we do observe that the composites with a larger CVF have a smaller averaged failure strain.

3.2. Data collection and machine learning

There are 25 microscale configurations generated at each CVF from 0% (metal only) to 100% (ceramic only) with 1% apart to collect data. Each simulation generates one data sample so that the collected dataset consists of 2525 data samples, in which the input feature is the CVF while the output targets include Young's modulus, Poisson's ratio, and failure strength. A few commonly used analytical formulas [Voigt (1887); Reuss (1929); Hashin and Shtrikman (1963)] that predict the material properties of composites are used here to validate the simulation results. Voigt [1887] assumed a uniform strain field to derive the effective mechanical properties of composite materials, while Reuss [1929] estimated the effective compliance tensor of composites by considering a uniform stress field. In another work, Hashin and Shtrikman [1963] (H-S) proposed the upper and lower bounds of elastic properties



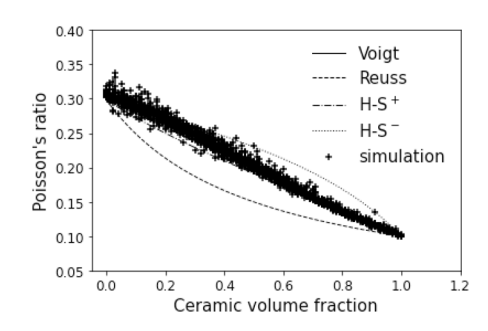
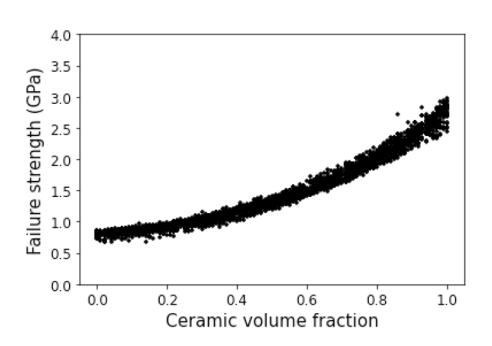


Fig. 9. Calculated material properties compared to the analytical solutions.



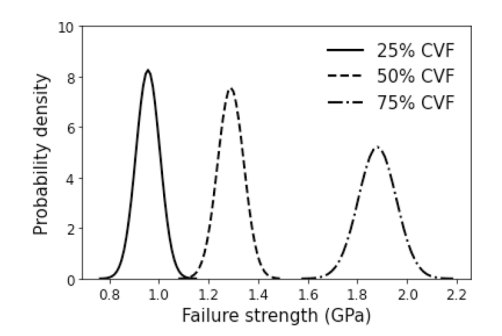


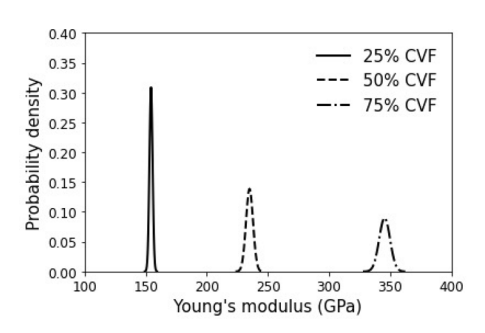
Fig. 10. Failure strength and its probability distributions at various CVFs.

of composites based on variational principles of the strain energy. Our calculated Young's modulus and Poisson's ratio fall in the range of those analytical solutions, as shown in Fig. 9, in which H-S+ and H-S- represent the upper and lower H-S bounds, respectively.

Figure 10 shows the collected data of failure strength. At a particular CVF, the failure strength follows the Gaussian distribution. Figure 10 also shows the probability distributions of composite failure strength at three different CVFs: 25%, 50%, and 75%. Obviously, the composite with a higher CVF has a higher mean failure strength and a larger standard deviation. The probability distributions of Young's modulus and Poisson's ratio are shown in Fig. 11. Averagely, the composite with a higher CVF has a higher Young's modulus and a smaller Poisson's ratio.

Three ML models are trained via GPR to predict Young's modulus, Poisson's ratio, and failure strength for the composite with a given CVF. The radial basis function is used as the kernel function in the regression models. The mean values and the 95% confidence intervals are shown in Fig. 12. It is important to note that GPR, as one of the Bayesian machine learning methods, does not learn a specific value for each input but rather a probability distribution over all real numbers. The predictions are sampled according to the learned probability distributions. In

Multiscale Modeling of Metal-Ceramic Spatially Tailored Materials



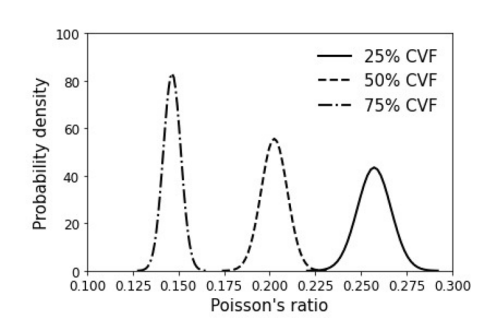
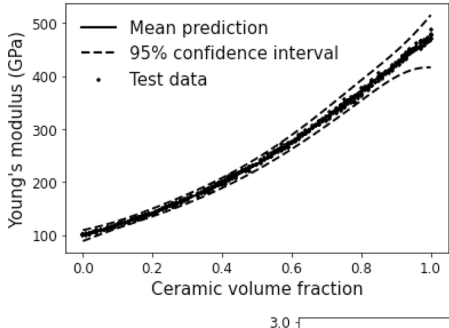
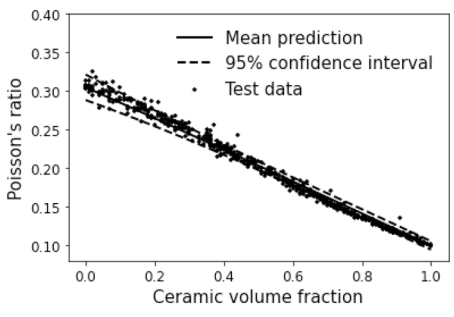


Fig. 11. The probability distributions of Young's modulus and Poisson's ratio at various CVFs.





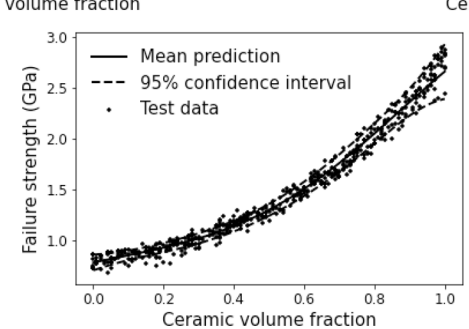


Fig. 12. Predictions of STM material properties from Gaussian Process Regression models compared to the test data.

- addition, the GPR shows higher variation around the boundaries (CVF is 0 or 1)
- due to the lack of data from the other side of the boundaries.

4. Macroscale Simulations

1

- 4 In macroscale peridynamic simulations, CVFs are assigned to each material point
- 5 according to the volume fraction distribution initialized in the simulation domain.
- 6 GPR models are applied to sample material properties, including Young's modulus,
- 7 Poisson's ratio, and failure strength, at each material point to generate various

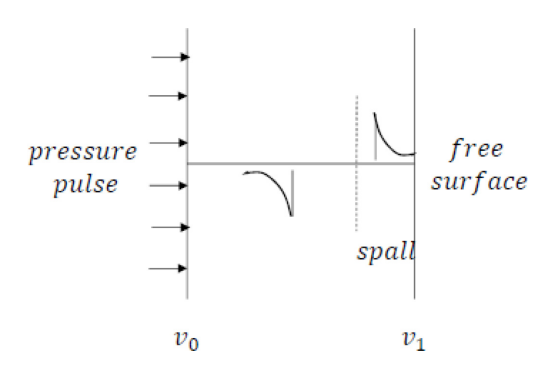


Fig. 13. Schematic description of spallation.

configurations. Monte Carlo simulations are conducted to study the mechanical behavior of metal-ceramic STM structures statistically.

4.1. Spallation in STM plates

In the first example, we study the spallation in Ti-TiB_2 STM plates with a thickness of 0.1 m, where the CVF varies along with the thickness. Spallation [Xiao (2006a)] is an interesting phenomenon of dynamic fracture, which occurs when shock waves interact to produce a region of tension in the interior of a material body. The spallation usually occurs under dynamic loadings, such as impact and explosion, as shown in Fig. 13. Here considers a pressure pulse, modeled via an exponential function in Eq. (19), to approximate the explosion on one surface of the STM plates.

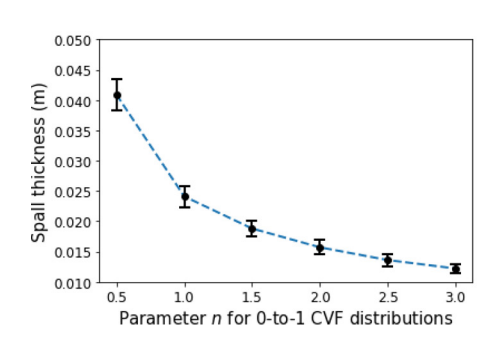
$$\sigma = \sigma_0 e^{-\beta t},\tag{19}$$

where $\sigma_0 = 1750 \,\mathrm{MPa}$ is the amplitude, and $\beta = 0.1567 \,\mathrm{s}^{-1}$.

Figure 13 demonstrates that once the pressure pulse applies on one surface of the plate, there is a compressive shock wave propagating towards another surface, which is a free surface. After being reflected by the free surface, the compressive wave becomes a tensile wave. If the magnitude of the tensile wave exceeds the tensile strength of the material during the wave propagation, spallation occurs. It shall be noted that the flux-corrected transport (FCT) algorithm [Xiao (2004); Xiao (2006a); Xiao (2006b)] is employed to maintain the strong discontinuity at the shock wavefronts.

We first consider that the CVFs are 0% at the loading surface (metal) and 100% at the free surface (ceramic), i.e., $v_0 = 0$ and $v_1 = 1.0$. Various metal-to-ceramic (or 0-to-1) CVF distributions can be determined via Eq. (1) once the parameter n is assigned. The metal-to-ceramic linear (n = 1), quadratic (n = 2), and square root (n = 0.5) distributions were plotted in Fig. 1. Three other nonlinear 0-to-1 CVF distributions (n = 1.5, n = 2.5, and n = 3.0) are also considered. A total of 800 simulations are conducted for each distribution. The calculated spall thicknesses and spall speeds follow the Gaussian distributions. The mean values with one standard

Multiscale Modeling of Metal-Ceramic Spatially Tailored Materials



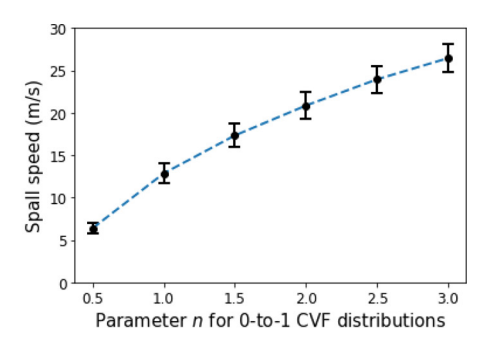
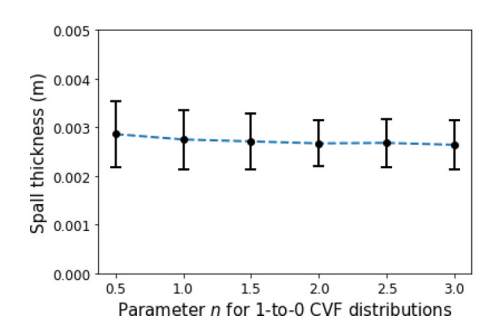


Fig. 14. Spall thickness and speed in plates with various metal-to-ceramic (0-to-1) CVF distributions with 97.5% confidential levels.



1

2

3

5

6

8

10

11

12

13 14

15

16

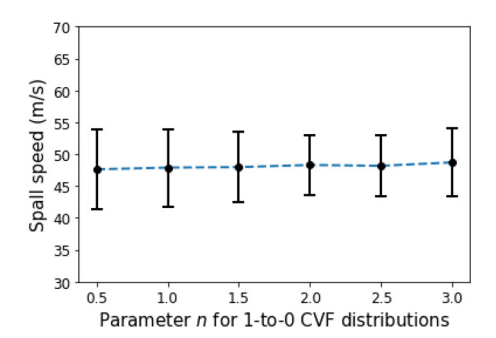


Fig. 15. Spall thickness and speed in plates with various ceramic-to-metal (1-to-0) CVF distributions with 97.5% confidential levels.

deviation of uncertainties are shown in Fig. 14. It can be seen that the plate with a 0-to-1 CVF distribution has a smaller mean spall thickness and a higher mean spall speed if the parameter n is larger. This is because a larger n results in a smaller CVF, as shown in Fig. 1, at the same location on the plates. Since STM has a lower failure strength at the location where the CVF is smaller, the spallation occurs earlier. Usually, a thin spall has a high speed.

We also design another type of STM plate with $v_0 = 1.0$ and $v_1 = 0$, i.e., 1-to-0 or ceramic-to-metal CVF distributions. In other words, the loading surface is ceramic, while the free surface is metal. Although we can conclude a similar statement as mentioned above about the effect of CVF distribution on spallation, there are no big differences in results, shown in Fig. 15. It is because the failure strength is not sensitive to small CVFs, as indicated in Figs. 10 and 12.

4.2. Fracture in STM plates with a hole

Several STM plates, with a hole at the center, are studied under uniaxial tension in the vertical direction. The plates are 30 mm by 30 mm in size, and the holes' diameters are 5 mm. Various CVF distributions are considered according to Eq. (2),

1 2

3

4

5

6

7

8

10

11

12 13

14

15

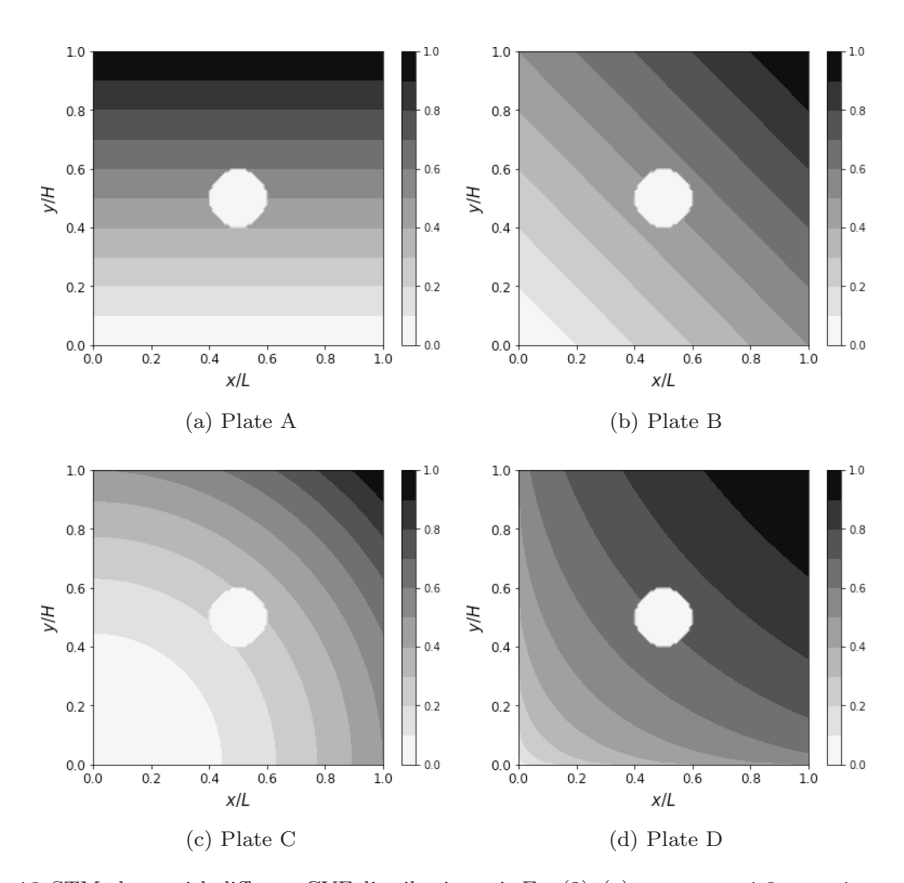


Fig. 16. STM plates with different CVF distributions via Eq. (2): (a) $n_x = n_y = 1.0, \eta_x = 1, \eta_y = 0$; (b) $n_x = n_y = 1.0, \eta_x = \eta_y = 0.5$; (c) $n_x = n_y = 2.0, \eta_x = \eta_y = 0.5$; and (d) $n_x = n_y = 0.5, \eta_x = \eta_y = 0.5$.

as shown in Fig. 16, in which two configurations have linear distributions while the other two have nonlinear distributions. After peridynamic models are generated, the material properties are predicted at each material point via the Gaussian process regressors. It shall be noted that even if two material points have the same CVF, they may have different material properties due to the uncertainties. Then, bond micromoduli and critical stretches between two material points in the peridynamic model are derived via mixing rule similarly as described in Sec. 3.1.

During the simulations, if a bond is elongated beyond its critical stretch, the bond is broken, and crack propagates. Figure 17 illustrates the deformed configuration after failures occur on the STM plates. It is observed that cracks propagate towards the regions with small CVFs because a smaller CVF generally results in a lower material failure strength and, in turn, a smaller bond critical stretch. The same conclusions were obtained in our recent work [Xiao et al. (2021)].

To investigate the uncertainty of failure stress, we have conducted 100 simulations for each type of plate. Table 2 lists the mean value and standard deviation of

2

3

6

8

9

10

11

12

Multiscale Modeling of Metal-Ceramic Spatially Tailored Materials

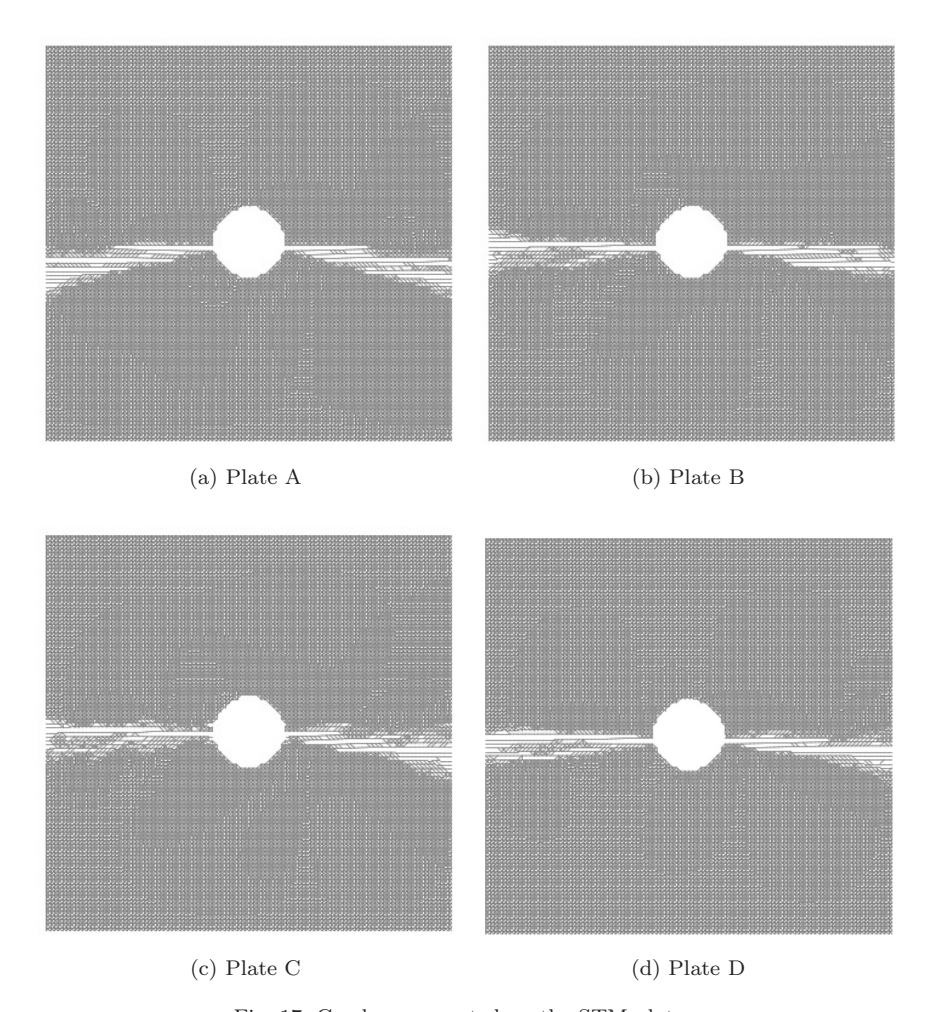


Fig. 17. Cracks propagated on the STM plates.

failure stress for STM plates. The table also includes the total CVF for each plate. It can be seen that Plate D has the highest mean failure stress while Plate C has the lowest mean failure stress. It is mainly because the total CVF of Plate D is the largest while the total CVF of Plate C is the smallest. Plates A and B have the same total CVF. However, due to the different distribution orientations, they have slightly different failure stresses. On the other hand, Plates B, C, and D have the same fracture pattern because the CVF distributions vary linearly or nonlinearly from 0 at the lower-left corner to 1 at the upper-right corner. However, the total CVFs are different, so material failures occur at various failure stresses listed in Table 2.

We also calculate the failure stresses of the same composite plates with uniform distributed particles. Therefore, the materials are considered homogeneous at the

Table 2. Failure stresses of STM plates.

	Plate A	Plate B	Plate C	Plate D
Mean (MPa) Standard deviation (MPa) Total CVF	680.7 11.1 50%	712.3 12.2 $50%$	573.2 25.9 33.8%	927.9 20.4 $66.3%$

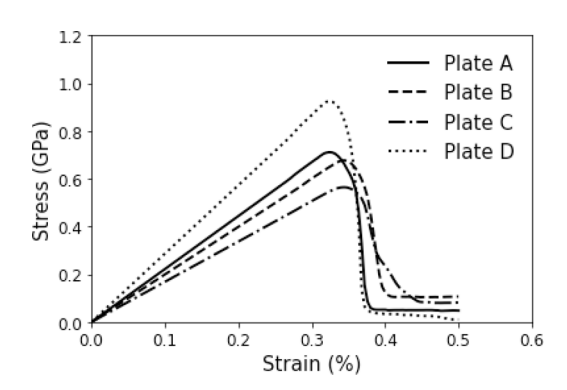


Fig. 18. Stress–strain relationships of STM plates under uniaxial tension.

macroscale, and the mean material properties are used. Assuming that the plates fail when the maximum stress at the hole reaches the tensile strength, we compute the failure stresses as 423 MPa, 505 MPa, and 643 MPa at the total CVFs of 33.8%, 50%, and 66.3%, respectively. It can be seen that STM plates B, C, and D reach much higher failure stresses than the corresponding homogeneous composite plates.

The stress–strain relationships are compared in Fig. 18 during the uniaxial tension on the STM plates. It can be seen that there are no big differences in failure strains between the STM plates. Plate D has a slightly lower failure strain, while Plate C has a slightly higher failure strain. Since ceramic (TiB₂) has a very low failure strain ($\sim 0.75\%$), the CVF variation has no significant impact on the failure strain of composites.

5. Conclusions

This study implemented a probabilistic ML model, GPR, in the ML-enhanced multiscale method to study metal—ceramic STMs. Peridynamics is utilized so that it is easy to generate computational models at the microscale with the consideration of microscale uncertainties, especially the uncertainty of porosity. It is observed that the material properties follow normal probability distributions at a specified volume fraction. The collected data is used to train GPR models that predict material properties based on the learned probability distribution. Then, the GPR models are implemented in macroscale peridynamic simulations to study the mechanics of STM structures. The effects of volume fraction distribution on the mechanical responses

- of STM structures are investigated. Such a multiscale approach can be extended to
- the design optimization of STM structures in future work.

3 Acknowledgments

- 4 This material is based upon work supported by the National Science Foundation
- 5 (#2104383) and US Department of Education (ED#P116S210005).

References

6

9

10

11

12

13

14

15

17

18

19

20

21

22

23

24

25

26

27

28

29

30

31

32

33

34

35

36

37

38

39

40

41

42

43

- 7 American Society for Metal [1979] Properties and Selection-Nonferrous Alloys and Pure 8 Metals: 1. Metals Park, 9th edn., Ohio, American Society for Metal.
 - Akshaya, S. L., Prakash, A. and Bharati Raj, J. [2021] "Applications of functionally graded materials in structural engineering: A review," *Lect. Notes Civ. Eng.* **97**, 553–566.
 - Alber, M., Buganza Tepole, A., Cannon, W. R. et al. [2019] "Integrating machine learning and multiscale modeling perspectives, challenges, and opportunities in the biological, biomedical, and behavioral sciences," NPJ Digit. Med. 2(1), 115.
 - Anitescu, C., Atroshchenko, E., Alajlan, N. et al. [2019] "Artificial neural network methods for the solution of second order boundary value problems," Comput. Mater. Contin. 59(1), 345–359.
 - Balokas, G., Czichon, S. and Rolfes, R. [2018] "Neural network assisted multiscale analysis for the elastic properties prediction of 3D braided composites under uncertainty," *Compos. Struct.* **183**, 550–562.
 - Birman, V., Chona, R., Byrd, L. W. et al. [2008] "Response of spatially tailored structures to thermal loading," J. Eng. Math. 61(2–4), 201–217.
 - Bobaru, F. and Zhang, G. [2015] "Why do cracks branch? A peridynamic investigation of dynamic brittle fracture," *Int. J. Fract.* **196**(1–2), 59–98.
 - Deierling, P. E. and Zhupanska, O. I. [2018] "Computational modeling of the effective properties of spatially graded composites," *Int. J. Mech. Sci.* **145**, 145–157.
 - Deierling, P. E., Zhupanska, O. I. and Pasiliao, C. L. [2021] "Spatial tailoring of a metal-ceramic composite panel subjected to high-speed flow," *J. Aerosp. Eng.* **34**(1), 04020093.
 - Gershman, S. J. and Blei, D. M. [2012] "A tutorial on Bayesian nonparametric models," J. Math. Psychol. 1, 1–12.
 - Ghaffari, M. A., Gong, Y., Attarian, S. and Xiao, S. [2019] "Peridynamics with corrected boundary conditions and its implementation in multiscale modeling of rolling contact fatigue," J. Multiscale Model. 10(1), 1841003.
 - Ghaffari, M. A., Zhang, Y. and Xiao, S. [2018] "Multiscale modeling and simulation of rolling contact fatigue," *Int. J. Fatique* **108**, 9–17.
 - Ghossein, E. and Lévesque, M. [2012] "A fully automated numerical tool for a comprehensive validation of homogenization models and its application to spherical particles reinforced composites," *Int. J. Solids Struct.* **49**(11–12), 1387–1398.
 - Hashin, Z. and Shtrikman, S. [1963] "A variational approach to the theory of the elastic behaviour of multiphase materials," *J. Mech. Phys. Solids* **11**(2), 127–140.
 - Izadi, R., Nayebi, A. and Ghavanloo, E. [2021] "Combined molecular dynamics—micromechanics methods to predict Young's modulus of fullerene-reinforced polymer composites," Eur. Phys. J. Plus 136, 816.
 - Jäkel, F., Schölkopf, B. and Wichmann, F. A. [2007] "A tutorial on kernel methods for categorization," J. Math. Psychol. **51**(6), 343–358.

- Jung, J. and Seok, J. [2016] "Fatigue crack growth analysis in layered heterogeneous material systems using peridynamic approach," *Compos. Struct.* **152**, 403–407.
 - Kanouté, P., Boso, D. P., Chaboche, J. L. et al. [2009] "Multiscale methods for composites: A review," Arch. Comput. Methods Eng. 16, 31–75.
 - Leonetti, L., Greco, F. and Trovalusci, P. et al. [2018] "A multiscale damage analysis of periodic composites using a couple-stress/Cauchy multidomain model: Application to masonry structures," Compos. B. Eng. 141, 50–59.
 - Liu, Z. and Wu, C. T. [2019] "Exploring the 3D architectures of deep material network in data-driven multiscale mechanics," *J. Mech. Phys. Solids* **127**, 20–46.
 - Liu, Z., Wu, C. T. and Koishi, M. [2019] "A deep material network for multiscale topology learning and accelerated nonlinear modeling of heterogeneous materials," Comput. Methods Appl. Mech. Eng. 345, 1138–1168.
 - Ly, D. K., Truong, T. T. and Nguyen-Thoi, T. [2022] "Multi-objective optimization of laminated functionally graded carbon nanotube-reinforced composite plates using deep feedforward neural networks-NSGAII algorithm," Int. J. Comput. Methods 19(3), 2150065.
 - Madenci, E. and Oterkus, S. [2016] "Ordinary state-based peridynamics for plastic deformation according to von Mises yield criteria with isotropic hardening," *J. Mech. Phys. Solids* 86, 192–219.
 - Morsi, K. and Patel, V. V. [2007] "Processing and properties of titanium-titanium boride (TiB_w) matrix composites-A review," J. Mater. Sci. **42**(6), 2037–2047.
 - Morsi, K. [2019] "Review: Titanium-titanium boride composites," J. Mater. Sci. 54(9), 6753–6771.
 - Munro, R. G. [2000] "Material properties of titanium diboride," J. Res. Natl. Inst. Stand. Technol. 105(5), 709–720.
 - Naebe, M. and Shirvanimoghaddam, K. [2016] "Functionally graded materials: A review of fabrication and properties," *Appl. Mater. Today* 5, 223–245.
 - Nishawala, V. V. and Ostoja-Starzewski, M. [2017] "Peristatic solutions for finite one- and two-dimensional systems," *Math. Mech. Solids* **22**(8), 1639–1653.
 - Patil, A. S., Hiwarkar, V. D., Verma, P. K. et al. [2019] "Effect of TiB₂ addition on the microstructure and wear resistance of Ti-6Al-4V alloy fabricated through direct metal laser sintering (DMLS)," J. Alloys Compd. 777, 165–173.
 - Reuss, A. [1929] "Berechnung der Fließgrenze von Mischkristallen auf Grund der Plastizittsbedingung für Einkristalle," ZAMM-J. Appl. Math. Mech./Zeitschrift für Angew. Math. und Mech. 9(1), 49–58.
 - Rohit, G. R. and Prajapati, J. M. and Patel, V. B. [2021] "Structural shape optimization by coupled FE–MM and swarm intelligence-based algorithm," *Int. J. Comput. Methods* **18**(4), 2050048.
 - Sahay, S. S., Ravichandran, K. S., Atri, R. et al. [1999] "Evolution of microstructure and phases in in situ processed Ti-TiB composites containing high volume fractions of TiB whiskers," J. Mater. Res. 14(11), 4214–4223.
 - Samaniego, E., Anitescu, C., Goswami, S. et al. [2020] "An energy approach to the solution of partial differential equations in computational mechanics via machine learning: Concepts, implementation and applications," Comput. Methods Appl. Mech. Eng. 362, 112790.
 - Schulz, Z., Speekenbrink, M. and Krause, A. [2018] "A tutorial on Gaussian process regression: Modelling, exploring, and exploiting functions," *J. Math. Psychol.* **85**, 1–16.
 - Shishkovsky, I., Kakovkina, N. and Sherbakov, V. [2017] "Graded layered titanium composite structures with TiB₂ inclusions fabricated by selective laser melting," *Compos. Struct.* **169**, 90–96.

8

9

10

11

12

13

14 15

16

17

18 19

20

21

22

23

24

25

26 27

28

29

30

31

32

33

34

35

36 37

38

39 40

41

42

43

44

45

- Silling, S. A. [2000] "Reformulation of elasticity theory for discontinuities and long-range forces," J. Mech. Phys. Solids 48(1), 175–209.
- 3 Silling, S. A. [2010] "Linearized theory of peridynamic states," J. Elast. 99(1), 85–111.
- Silling, S. A. and Askari, E. [2005] "A meshfree method based on the peridynamic model of solid mechanics," *Comput. Struct.* **83**(17–18), 1526–1535.
 - Silling, S. A. and Askari, A. [2014] Peridynamic Model for Fatigue Cracking, Technical Report.
 - Silling, S. A., Epton, M., Weckner, O. et al. [2007] "Peridynamic states and constitutive modeling," J. Elast. 88(2), 151–184.
 - Silling, S. A. and Lehoucq, R. B. [2010] Peridynamic Theory of Solid Mechanics, Elsevier.
 Trovalusci, P., Capecchi, D. and Ruta, G. [2009] "Genesis of the multiscale approach for materials with microstructure," Arch. Appl. Mech. 79, 981.
 - Trovalusci, P., De Bellis, M. L. and Masiani, R. [2017] "A multiscale description of particle composites: From lattice microstructures to micropolar continua," *Compos. B. Eng.* **128**, 164–173.
 - Voigt, W. [1887] "Theoretische Studien über die Elasticitätsverhältnisse der Krystalle. I," Abhandlungen der Königlichen Gesellschaft der Wissenschaften Göttingen 34, 3–52.
 - Wang, K. and Sun, W. C. [2018] "A multiscale multi-permeability poroplasticity model linked by recursive homogenizations and deep learning," Comput. Methods Appl. Mech. Eng. 334, 337–380.
 - Wang, C., Deng, A., Taheri, A. et al. [2020] "A mesh-free approach for multiscale modeling in continuum–granular systems," Int. J. Comput. Methods 17(10), 2050006.
 - White, D. A., Arrighi, W. J., Kudo, J. et al. [2019] "Multiscale topology optimization using neural network surrogate models," Comput. Methods Appl. Mech. Eng. 346, 1118–1135.
 - Wiley, D. E., Manning, W. R. and Hunter, O. [1969] "Elastic properties of polycrystalline TiB₂, ZrB2 and HfB2 from room temperature to 1300K," *J. Less Common Met.* **18**(2), 149–157.
 - Xiao, S. [2004] "An FE-FCT method with implicit functions for the study of shock wave propagation in solids," *Wave Motion* **40**(3), 263–276.
 - Xiao, S. [2006] "A non-oscillatory method for spallation studies," Int. J. Numer. Methods Eng. 66, 364–380.
 - Xiao, S. [2006] "A lattice Boltzmann method for shock wave propagation in solids," *Commun. Numer. Methods Eng.* **23**(1), 71–84.
 - Xiao, S., Deierling, P., Attarian, S. et al. [2021] "Machine learning in multiscale modeling of spatially tailored materials with microstructure uncertainties," Comput. Struct. 249, 106511.
 - Xiao, S. and Hou, W. [2007] "Studies of nanotube-based aluminum composites using the bridging domain coupling method," *Int. J. Multiscale Comput. Eng.* **5**(6), 447–459.
 - Xiao, S., Hu, R., Li, Z. et al. [2019] "A machine-learning-enhanced hierarchical multiscale method for bridging from molecular dynamics to continua," Neural Comput. Appl. 9, 1–15.
 - Xiao, S., Wang, S., Ni, J. et al. [2008] "Reliability analysis of carbon nanotubes using molecular dynamics with the aid of grid computing," J. Comput. Theor. Nanosci. 5(4), 528–534.
 - Xiao, S. and Yang, W. [2006] "Temperature-related Cauchy–Born rule for multiscale modeling of crystalline solids," *Comput. Mater. Sci.* **37**(3), 374–379.
- Xiao, S. and Yang, W. [2007] "A temperature-related homogenization technique and its implementation in the meshfree particle method for nanoscale simulations," Int. J. Numer. Methods Eng. 69(10), 2099–2125.

- Xing, W. and Miller, A. D. [2021] "A multiscale failure modeling framework for strain localization in quasi-brittle materials," *Int. J. Comput. Methods* **18**(10), 2150045.

 Yaghoobi, A. and Chorzepa, M. G. [2017] "Fracture analysis of fiber reinforced concrete
- Yaghoobi, A. and Chorzepa, M. G. [2017] "Fracture analysis of fiber reinforced concrete structures in the micropolar peridynamic analysis framework," *Eng. Fract. Mech.* **169**, 238–250.
- Yang, W. and Xiao, S. [2008] "Extension of the temperature-related Cauchy–Born rule:
 Material stability analysis and thermo-mechanical coupling," *Comput. Mater. Sci.*41(4), 431–439.
- Zhu, Q. Z. and Ni, T. [2017] "Peridynamic formulations enriched with bond rotation effects," Int. J. Eng. Sci. 121, 118–129.